Secondary instability development in the post-buckling regime in soft composites

Secondary Instability Development in the Post-Buckling Regime in Soft Composites

Dean Chen[a], Yuhai Xiang[b], Nitesh Arora[a], Qi Yao[a], Jian Li[c,d], and Stephan Rudykh[e]*

[a] *Department of Mechanical Engineering, University of Wisconsin–Madison, WI 53706, United States*
[b] *Department of Chemical Engineering and Materials Science, University of Minnesota, Minneapolis, 55455, Minnesota, United States*
[c] *Joint International Research Laboratory of Key Technology for Rail Traffic Safety, Central South University, Changsha, 410075, China*
[d] *Department of Civil and Environmental Engineering, Massachusetts Institute of Technology, Cambridge, MA 02139, United States*
[e] *School of Mathematical and Statistical Sciences, University of Galway, University Road, Galway, Ireland*

∗ Corresponding author. E-mail address: rudykh@wisc.edu (S. Rudykh).

Abstract

In this paper, we report the numerical observations of a distinctive phenomenon – the development of *secondary* buckling in soft particulate composites. After experiencing the first microstructural buckling event and consequent microstructure transformations, the composite re-enters a stable state. However, the composite may undergo a secondary buckling upon exceeding a certain deformation level. This secondary buckling event gives rise to a plethora of distinct instability patterns and behaviors. We conduct the finite-amplitude post-buckling and Bloch Floquet analyses implemented in the post-buckling regime to characterize the development of the secondary buckling. These analyses also characterize the dependence of the critical strain and wavelength of the secondary buckling on the composite's initial microstructure parameters.

1. Introduction

Soft composites can experience elastic instabilities under large deformations (Li et al., 2021), leading to microstructure transformations that enable the design of materials with tunable and switchable properties. Examples include acoustic materials with tunable bandgaps (Li et al., 2019c; Rudykh & Boyce, 2014; Shan et al., 2014; Wang et al., 2014; Gao et al., 2019), and negative group velocity states (Slesarenko et al., 2018, Arora et al. 2022), and the mechanical metamaterials exhibiting auxetic behaviors (Bertoldi et al., 2010; Mullin et al., 2007; Li et al., 2018b, Li et al., 2019b, Li et al., 2019c). Furthermore, instability-induced microstructure transformations can also be utilized to design soft active robotics (Rafsanjani et

al., 2021).

To detect the onset of elastic instabilities, two analysis frameworks are typically employed. The first is the "small-on-large" framework (Ogden, 1997), which examines linearized, infinitesimal perturbations superimposed on a finitely deformed configuration. In this framework, macroscopic (or longwave) instabilities are typically identified by the loss of ellipticity analysis. In composite materials, the analysis requires the evaluation of the effective tensor of instantaneous elastic moduli, which can be calculated through numerical (Bruno et al., 2010; Greco & Luciano, 2011; Greco et al., 2018, 2021; Pranno et al., 2022; De Maio et al., 2023; Aboudi & Gilat, 2023; Melnikov et al., 2021) or analytical (Rudykh & Debotton, 2012) homogenization approaches, or, alternatively, from phenomenological models (Merodio & Ogden, 2002, 2003, 2005a, 2005b; Merodio & Pence, 2001a, 2001b; Aboudi & Volokh, 2020; Ehret & Itskov, 2007; Volokh, 2017; Qiu & Pence, 1997). For analyzing the so-called microscopic instabilities developing at finite wavelengths (Geymonat et al., 1993), more demanding approaches, typically the Bloch-Floquet analysis and its alternatives, are usually employed (Geymonat et al., 1993; Triantafyllidis et al. 2006; Bertoldi et al., 2008). The second framework addresses finite-amplitude deformations in the post-buckling regime (Okumura et al., 2002; Li et al., 2019c). Such analyses are typically performed with the finite-element method on either finite samples or sufficiently large periodic representative volumes.

The application of the analysis method depends on the composite's geometric configuration. If the material's initial primitive cell allows arbitrary enlargement along the buckling direction (a "continuous-buckling" composite in our terminology), the resulting instabilities can be effectively analyzed using Bloch–Floquet methods. This category includes soft layered materials and fiber composites when loaded along their primary direction. For soft layered materials, Li et al. (2013) observed both micro- and macroscopic instabilities in 3D-printed layered materials. Slesarenko and Rudykh (2016) achieved tunable wavy patterns in soft laminates with visco-hyperelastic behaviors (Xiang et al., 2020a, 2020b) by manipulating the strain rates. Li et al. (2019d) analyzed the elastic instability of compressible laminates and observed the stabilizing influence of phase compressibility. Li et al. (2022) experimentally observed the instability-driven formation of twinning microstructures in soft laminates. For fiber composites (FCs), Galich et al. (2018) investigated the influence of periodic fiber

distribution in 3D composites on their instabilities and shear wave propagation. Via micromechanics-based homogenization, Rudykh & Debotton (2012) predicted the macroscopic instabilities in transversely isotropic fiber composites. Li et al. (2018a) experimentally observed elastic instabilities in 3D-printed fiber composites, which shows a transition from small wavelength wavy patterns to longwave modes. Arora et al. (2022b) analyzed the influence of constituent material properties on the orientation of buckling in fiber composites through both simulations and experiments.

In contrast, some composites have initial primitive cells with a well-defined period length along the buckling direction (a "discrete-buckling" composite in our terminology), including porous materials (Bertoldi et al., 2008), particulate composites (Goshkoderia et al., 2020), and honeycomb lattices (Papka & Kyriakides, 1999a, 1999b; Okumura et al., 2002). In these composites, the small-on-large framework still applies if buckling is commensurate (wavelength is an integer multiple of the primitive-cell period) or intracell (develops within the primitive cell; Combescure et al., 2016). However, when buckling is incommensurate, linearized predictions often diverge from the ensuing finite-amplitude evolution; a post-buckling analysis is therefore required to capture the actual developing mode (Chen et al., 2023).

Particulate composites are a typical and important class of "discrete-buckling" composites, in which discretely placed stiff particles are embedded in a soft matrix. Triantafyllidis et al. (2006) investigated the instabilities in particulate composites containing periodic circular stiff inclusions subjected to combined in-plane loadings. Li et al. (2019a) experimentally observed the formation of wavy chain patterns in soft particulate composites. Xiang et al. (2023) examined the interplay between viscoelasticity and instabilities in soft particulate composites undergoing finite deformation. However, the divergence between the linearized predictions and the post-buckling evolution during large-path deformation was not examined in those studies. Recent sequential studies on instabilities in particulate composites have revealed distinctive behaviors from the first onset of buckling to large-deformation post-buckling regimes. The first work in this series (Chen et al., 2022) observed a divergence between the Bloch–Floquet predictions and the actual post-buckling behavior in soft particulate composites, showing that the instability characteristics couple strongly on inclusion size and distribution. The subsequent work (Chen et al., 2023) quantitatively characterized this post-buckling evolution,

demonstrating that the initially formed instability patterns undergo complex morphological transformations due to incommensurate buckling over well-defined primitive cells. To accurately capture the post-buckling response, a Discrete Fourier Transform (DFT)-based post-processing method was developed and applied to extract the critical characteristics.

However, neither prior studies in this series nor existing reports have observed secondary instabilities in soft particulate composites under continued loading. The challenge is that secondary buckling typically requires the first buckling mode to retain (or restore) certain structural stiffness. In particulate composites, particle interactions are mediated by a soft matrix, yielding a weakly connected network—unlike honeycomb lattices or laminates, where the stiff phase forms the stem network. As a result, particulate composites have generally been expected to lose stiffness progressively, making secondary buckling unlikely to develop. However, building on this series of studies, we identify a special first-buckling mode—periodicity-doubling (Chen et al., 2023)—that can partially and rapidly restore stiffness after the first instability, thereby creating conditions conducive to secondary buckling. To examine this possibility, we perform finite-amplitude post-buckling analyses on sufficiently large samples to capture transitions from periodicity-doubling into a secondary-buckling regime. We then apply Discrete Fourier Transform (DFT) to extract the corresponding critical characteristics and finally conduct Bloch–Floquet (BF) analyses on the post–first-buckling configurations to compare with the finite-amplitude post-buckling results.

2. Theoretical background

We consider a finitely deformed continuum body, in which each material point is identified by the position vector $\boldsymbol{X}$ in the reference (or undeformed) configuration, and $\boldsymbol{x}$ in the current (or deformed) configuration. The displacement of the material point is described by the mapping relation $\boldsymbol{x} = \chi(\boldsymbol{X})$, while the deformation gradient is defined as $\boldsymbol{F} = \partial \boldsymbol{x}/\partial \boldsymbol{X}$. The determinant of the deformation gradient $J \equiv det\, \boldsymbol{F} > 0$ represents the local volume change between the deformed and the undeformed configurations. In this study, we consider hyperelastic behavior of materials, where the stress response is derived from a strain energy density function, $W(\boldsymbol{F})$. The first Piola-Kirchhoff stress tensor is obtained via

$$\boldsymbol{P} = \frac{\partial W(\boldsymbol{F})}{\partial \boldsymbol{F}}. \tag{1}$$

For incompressible materials, $J = 1$, introducing an additional constraint, and the associated unknown Lagrange multiplier (pressure-like term) p, thus Eq. (1) is modified as

$$\boldsymbol{P} = \frac{\partial W(\boldsymbol{F})}{\partial \boldsymbol{F}} - p\boldsymbol{F}^{-T}. \tag{2}$$

The Cauchy stress tensor ($\boldsymbol{\sigma}$) is related to the first Piola-Kirchhoff stress tensor via,

$$\boldsymbol{\sigma} = J^{-1}\boldsymbol{P}\boldsymbol{F}^{T}. \tag{3}$$

The quasi-static equilibrium condition can be expressed in the reference configuration as:

$$Div\, \boldsymbol{P} = \boldsymbol{0}, \tag{4}$$

in the absence of body forces.

The instability analysis is addressed by superimposing small incremental deformations on a finitely deformed state (Ogden, 1997), which gives the incremental form of the constitutive law:

$$\dot{\boldsymbol{P}} = \mathbb{A} : \dot{\boldsymbol{F}}, \tag{5}$$

where $\dot{\boldsymbol{F}} = Grad\, \dot{\boldsymbol{u}}$ describes the gradient of the incremental displacement field $\boldsymbol{u}$, and $\mathbb{A}$ is the fourth-order effective tensor of instantaneous elastic moduli governing the incremental response, expressed as

$$\mathbb{A} = \frac{\partial^2 W}{\partial \boldsymbol{F} \partial \boldsymbol{F}}. \tag{6}$$

For incompressible materials, the incremental incompressibility constraint is expressed as:

$$tr(\dot{\boldsymbol{F}}\boldsymbol{F}^{-1}) = 0. \tag{7}$$

In the homogenized setting with the materials characterized by its effective properties, and undergoing homogenous deformation, $\mathbb{A}_{i\alpha j\beta}$ is independent of $\boldsymbol{X}$. Then, the incremental equilibrium equation can finally be written as,

$$\mathbb{A}_{i\alpha j\beta} \frac{\partial^2 \dot{u}_j}{\partial X_\alpha \partial X_\beta} - \frac{\partial \dot{p}}{\partial X_i} = 0, \tag{8}$$

where $\dot{p}$ is an incremental change in p.

We seek a solution for Eq.(8) in the form

$$\dot{\boldsymbol{u}} = \hat{\boldsymbol{m}} e^{ik\boldsymbol{x}\cdot\hat{\boldsymbol{n}}},\ \dot{p} = \hat{p} e^{ik\boldsymbol{x}\cdot\hat{\boldsymbol{n}}}, \tag{9}$$

where k is a wavenumber, $\hat{\boldsymbol{m}}$ and $\hat{\boldsymbol{n}}$ are unit vectors.

Substituting Eq. (9) into Eq. (8) yields

$$\boldsymbol{Q}\hat{\boldsymbol{m}} + i\hat{p}\hat{\boldsymbol{n}} = \boldsymbol{0}, \tag{10}$$

where $\boldsymbol{Q}$ is the acoustic tensor with components defined as $Q_{ij} = \mathbb{A}^0_{ipjq}\hat{n}_p\hat{n}_q$.

Longwave (or macroscopic) instability occurs when the strong ellipticity condition,

$$Q_{ij}\hat{m}_i\hat{m}_j \equiv \mathbb{A}^0_{ipjq}\hat{n}_p\hat{n}_q\hat{m}_i\hat{m}_j > 0, \tag{11}$$

is violated. Specifically, along a loading path, the first point that gives the loss of ellipticity condition, namely, $Q_{ij}\hat{m}_i\hat{m}_j = 0$, is identified as the onset of longwave instability. In periodic material structures, instabilities may also develop at length scales comparable with the microstructures (namely, the microscopic instabilities). Therefore, a refined approach, Bloch-Floquet analysis (Bertoldi et al., 2008) in the framework of small amplitude deformations superimposed on finite deformation, is employed to capture both macroscopic and microscopic instability modes. As an alternative to this linearized approach, the post-buckling analysis considers the nonlinearity in the emerging post-buckling development, thus, providing additional information about the further evolution of instability patterns in the post-buckling regime (Chen et al. 2023).

As the focus of this research, the potential secondary instability is expected to develop in the post-buckling regime, after the occurrence of the first buckling. Two complementary frameworks can be employed to analyze the secondary instability: (i) the finite-amplitude development analysis, and (ii) the small-amplitude linearized analysis superimposed on the finitely deformed state, which correspond to the post-buckling and Bloch–Floquet analyses, respectively, in this study. Both methods are implemented on the post-buckling state, and their results are complementary for understanding the development of instability. However, the two analyses may diverge. The Bloch–Floquet analysis is based on a linearized analysis along the loading path; however, the development of the initial buckling configuration with further deformation, may result in a loss of stability along the loading path, and the configuration may further evolve and adapt into a stable configuration in the post-buckling regime. This nonlinear adaptation can lead to discrepancies between the predictions of these methods. In this study, we shall examine whether such divergence occurs for the secondary buckling of soft particulate composites.

3. Numerical simulation

We construct a 2D periodic particulate composite with a single circular stiff inclusion located at the center of a rectangular primitive unit cell (as illustrated in Fig. 1). The width and length of the primitive unit cell are denoted by a and b, respectively. The diameter of the circular inclusion is represented by d. The initial configuration of the unit cell can be completely determined through two parameters: the periodicity aspect ratio $\eta = a/b$ and the inclusion spacing ratio $\xi = d/b$.

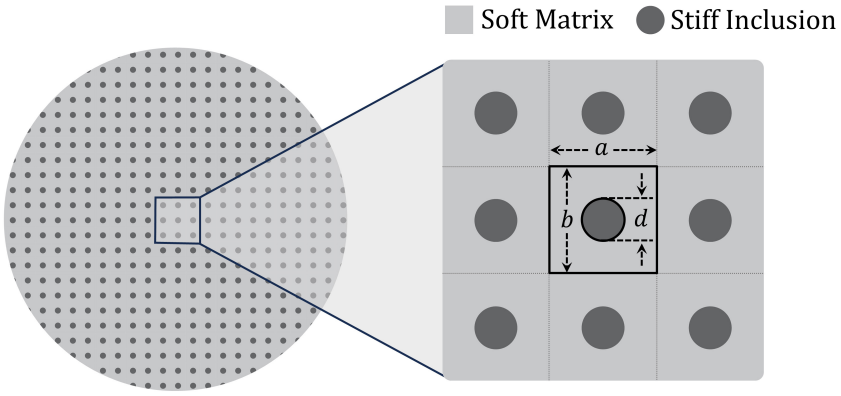

Fig. 1 Schematic composite microstructure with stiff circular inclusions periodically distributed in soft matrix.

The behavior of the stiff inclusion and soft matrix is described by hyperelastic models. In particular, we employ a nearly incompressible neo-Hookean strain energy density function, namely,

$$\mathrm{W}^{(q)} = \frac{\mu^{(q)}}{2}(I_1 - 3) + \frac{\kappa^{(q)}}{2}(J-1)^2, \tag{12}$$

where $\mu^{(q)}$ and $\kappa^{(q)}$ represent the initial shear modulus and bulk modulus, respectively; $I_1 = \mathrm{tr}\boldsymbol{C}$ is the first invariant of the right Cauchy-Green tensor, where $\boldsymbol{C} = \boldsymbol{F}^{\mathrm{T}}\boldsymbol{F}$. To differentiate the material properties of various phases, a superscript (q) is used for each parameter. For instance, $(q) = (i)$ and $(q) = (m)$ denote the material properties of the stiff inclusion and soft matrix, respectively. We set the inclusion-to-matrix ratio of the shear moduli to be $\mu^{(\mathrm{i})}/\mu^{(\mathrm{m})} = 10^3$. Due to this high modulus contrast, the local deformation of the stiff inclusions under macroscopic compression is negligible, and the majority of the macroscopic deformation is accommodated by the local deformation of the soft matrix. To maintain nearly incompressible material behavior in numerical simulation, a high ratio $\Lambda = \frac{\kappa^{(q)}}{\mu^{(q)}} = 10^3$ is

assigned to both soft and stiff materials.

We first employ finite amplitude analysis, essentially a post-buckling analysis, of secondary instability in Sec. 3.1. Independently, we identify first-stage buckling modes that contain an integer number of inclusions and are capable of developing secondary buckling. Based on the corresponding RVE, we then apply a small amplitude linearized analysis using the Bloch–Floquet technique. Both methods are implemented in the post-buckling regime and serve as complementary approaches to analyze secondary instability. The detailed procedures of the two analyses are described in Secs. 3.1 and 3.2, respectively. We implement both analyses using the finite element code in COMSOL Multiphysics 6.0.

3.1 Finite-amplitude post-buckling analysis

We construct a representative volume element (RVE) (Bertoldi et al., 2008, Chen et al., 2023) as shown in Fig. 2. The RVE is constructed with a size of 320×1, representing a single column of $\mathrm{N} = 320$ composite unit cells, which enables the development of post-buckling patterns with a wide range of wavelengths. The RVE is enclosed by four boundaries (AB, CD, AC, and BD), defined by nodes $A, B, C,$ and D. The in-plane unidirectional compression is applied via periodic boundary conditions imposed on the boundary pair $AB - CD$ and $AC - BD$ as

$$\boldsymbol{u}_{src} - \boldsymbol{u}_{dst} = (\overline{\boldsymbol{F}} - \boldsymbol{I})(\boldsymbol{X}|_{src} - \boldsymbol{X}|_{dst}) = \overline{\boldsymbol{H}}(\boldsymbol{X}|_{src} - \boldsymbol{X}|_{dst}), \tag{13}$$

where $\boldsymbol{u}_{src}$ and $\boldsymbol{u}_{dst}$ denote the displacement vector of an arbitrary pair of points periodically located on the source and destination boundary of the boundary pair, respectively; $\overline{\boldsymbol{F}}$ is the average deformation gradient, $\boldsymbol{I}$ is the identity tensor and $\overline{\boldsymbol{H}} = \overline{\boldsymbol{F}} - \boldsymbol{I}$ denotes the average displacement gradient. The unidirectional compression is applied in the direction of $\boldsymbol{e}_2$ via prescribing the displacement gradient as

$$\overline{\boldsymbol{H}} = (\lambda_1 - 1)e_1 \otimes e_1 + (\lambda_2 - 1)e_2 \otimes e_2, \tag{14}$$

where λ_1 and λ_2 denote the principal stretch ratios in the direction of $\boldsymbol{e}_1$ and $\boldsymbol{e}_2$, respectively. We apply the compression defined by the average compressive strain $\varepsilon = 1 - \lambda_2$, where λ_1 is constrained by $\lambda_1\lambda_2 = 1$ to ensure material incompressibility. As a perturbation to trigger instabilities, geometrical imperfection with an amplitude of $10^{-5}d$ is introduced in terms of a slight alternation of the shape and position of the stiff inclusions (Chen et al., 2023,

Appendix C). Specifically, the inclusions are modeled as nearly circular ellipses, where the random geometrical differences are introduced independently onto the shape, dimension, and center position of each inclusion.

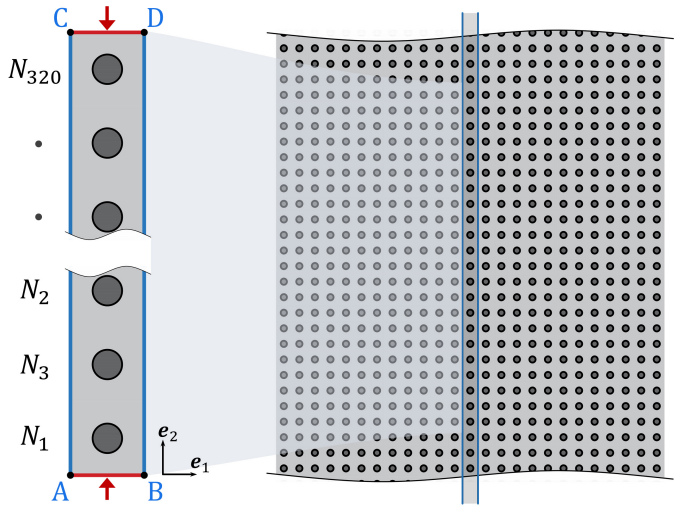

Fig. 2 Schematic representative volume element ($N \times 1$) with periodically distributed number $N = 320$ of composite unit cells in a column used for finite-amplitude post-buckling analysis.

To capture the onset of secondary buckling and to identify the corresponding critical wavenumber, we utilized a post-processing method that characterizes the post-buckling structure obtained from FEA via discrete Fourier transformation (DFT) (Chen et al., 2023). Specifically, we track the position of the inclusion centers throughout the first and the secondary buckling. This procedure starts with building a representation of a "chain" of stiff inclusions by a sequence of coordinates corresponding to the inclusions' center position. Note that the shape deformation of the stiff inclusions is negligible. Next, we apply a discrete Fourier transform (DFT) on the obtained sequence of coordinates to find its wavenumber components and corresponding Fourier coefficient. Given a sequence of coordinates being defined at the center positions of the inclusions, namely, $\{x_n\} := x_1, x_2, x_3 \dots, x_N$ in $\boldsymbol{e}_1$ direction and $\{y_n\} := y_1, y_2, y_3 \dots, y_N$ in $\boldsymbol{e}_2$ direction. If $\{y_n\}$ is normalized via $\{y_n\}_{norm} = \{y_n\}/\lambda b$, the sequence of inclusions' center coordinates becomes $\{n, x_n\}$ given that the vertical distance between vertically adjacent inclusions remains nearly constant in all our considered cases. In our analysis, the discrete Fourier transform (DFT) reassembles the sequence of inclusion center coordinates $\{x_n\}$, via a sequence of harmonic coordinate sets based on a fundamental

wavenumber $1/N$, where N is the number of inclusions in the RVE, and K/N is the corresponding wavenumber of the Kth harmonic set of coordinates. By solving the linear equation system:

$$x_n = \sum_{K=0}^{N-1} f_K \cdot e^{i2\pi \frac{K}{N} n}, \tag{15}$$

we finally obtain the dependence of the Fourier coefficient f_K on the corresponding component wavenumber $k = K/N$, namely, the wavenumber spectrum $f_K = F(k)$, where $(k = 1/N,\ 2/N, ...,\ (N-1)/N,\ 1)$.

Next, we identify the peak point in the wavenumber spectrum $f_K = F(k)$ (corresponding to the harmonic set of coordinates that dominates the post-buckling pattern) as the critical wavenumber. This results from the buckling wavelength being significantly larger than the size of the RVE. Note that, with a finite-sized RVE, the DFT analysis identifies the longwave instabilities at the lowest wavenumber ($k = 1/320$) in the scanned range, so that the wavelength of the buckling pattern is equal to the height of the RVE. Similarly, if a larger number of unit cells in the RVE is used (for example, 640 cells), the critical wavelength will increase to $l^{cr} = 640$ and the corresponding critical wavenumber shifts down to $k = 1/640$.

3.2 Bloch-Floquet analysis in the post-buckling regime

To analyze the onset of secondary buckling, we can also superimpose a Bloch-Floquet analysis on the deformed RVE in the post-buckling regime after the first stage buckling. However, in our considered cases, not all post-buckling structures can develop secondary buckling. We observe that secondary buckling occurs only when the first-stage buckling mode corresponds to an integer enlargement of the composite's initial periodicity. Otherwise, a mismatch between the buckling wavelength and the discrete spacing of the stiff inclusions accumulates, causing the particles to distribute along an "inclined" line relative to the direction of compression. This prevents the formation of a reinforced layer aligned with the compression direction and thereby suppresses the development of secondary buckling. As shown by Chen et al. (2023), such integer enlargement of wavelength, in practice, occurs only when the first-stage buckling mode exactly doubles the initial periodicity, referred to as the "periodicity-doubling" mode. It is important to note that this "periodicity-doubling" mode also includes the so-called

"adapted periodicity-doubling" mode (see Fig. 8), which cannot be predicted by Bloch–Floquet analysis but can be captured by DFT analysis of the post-first-stage buckling state (Chen et al., 2023). In summary, for all our considered cases, this "periodicity-doubling" mode is the only one found to further develop secondary instability.

Therefore, we consider an initial RVE consisting of two composite unit cells (see Fig. 3a), and derive its post-buckling state (see Fig. 3b) using the same method stated in sec 3.1. Next, we superimpose Bloch–Floquet analysis on the post-buckling state of RVE corresponding to the "periodicity-doubling" state. The Floquet periodic conditions relate the incremental displacement fields u via

$$\boldsymbol{u}(\boldsymbol{X}+\boldsymbol{R}) = \boldsymbol{u}(\boldsymbol{X})e^{i\boldsymbol{K}\cdot\boldsymbol{R}}, \tag{16}$$

where $\boldsymbol{R} = \boldsymbol{R}_1 a\boldsymbol{e}_1 + \boldsymbol{R}_2(Nb)\boldsymbol{e}_2$ denotes a vector corresponding to the composite's initial periodicity (R_1 , R_2 are arbitrary integers), and $\boldsymbol{K} = K_1\boldsymbol{e}_1 + K_2\boldsymbol{e}_2$ represents the superimposed Bloch wave vector. In FEA, the Floquet boundary conditions, $\boldsymbol{u}_{ab} = \boldsymbol{u}_{cd}e^{-i\boldsymbol{K}\cdot(\boldsymbol{R}_{ab}-\boldsymbol{R}_{cd})}$ and $\boldsymbol{u}_{bd} = \boldsymbol{u}_{ac}e^{-i\boldsymbol{K}\cdot(\boldsymbol{R}_{bd}-\boldsymbol{R}_{ac})}$, are imposed on the boundary pairs $ab-cd$ and $bd-ac$ of the primitive unit cell. Then, the Bloch–Floquet analysis is conducted by solving the corresponding eigenvalue problem. Here, we normalize the components of the wavenumber as $k_1 = K_1 a/2\pi$ and $k_2 = K_2(Nb)/2\pi$ in the undeformed configuration. Finally, we identify the occurrence of the secondary buckling at the lowest strain level (namely, the critical strain ε_{II}^{cr}) while a zero eigenvalue emerges at a critical wavenumber k^{cr} (k_1^{cr} or k_2^{cr}). The cases with $k^{cr} \to 0$ are referred to as the "longwave" or "macroscopic instability", while cases with $k^{cr} > 0$ are referred to as the "microscopic instabilities". Throughout our calculation, we observe that the secondary buckling is found to develop only in the direction of compression (the direction of $\boldsymbol{e}_2$). Therefore, here and thereafter in this paper, we report the corresponding critical wavenumber of the secondary buckling as $k_{II}^{cr} = k_2^{cr}$, where the subscript "II" denotes the critical characteristics of the secondary buckling, and "I" denotes those of the first stage buckling.

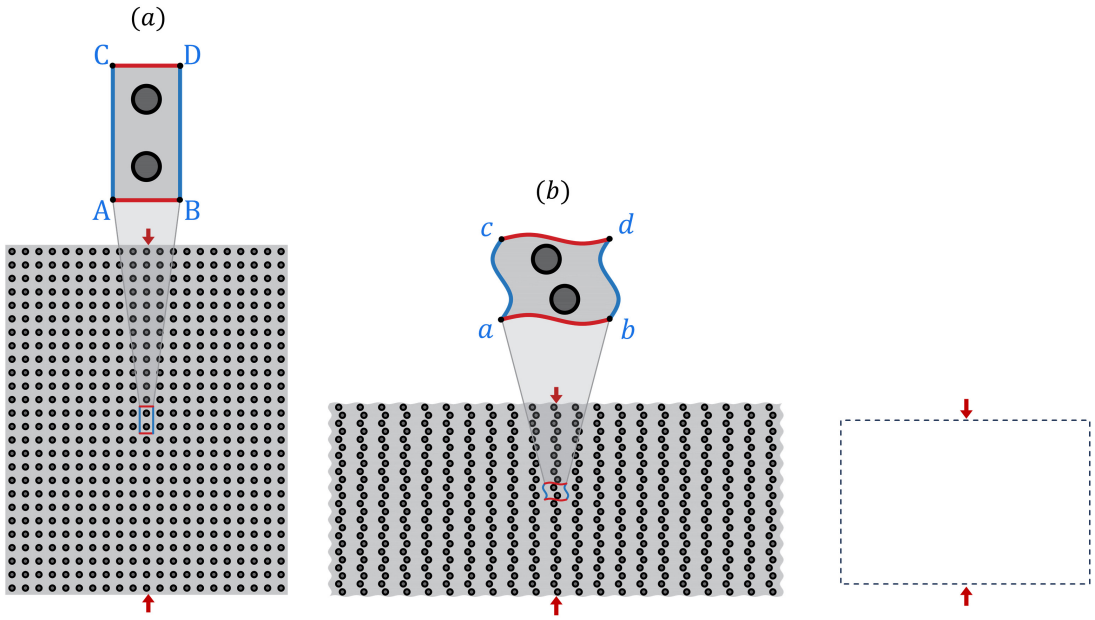

Fig. 3 Schematic representative volume element consisting of two composite unit cells in the a) undeformed and b) post buckling state with "periodicity-doubling" mode for the Bloch-Floquet analysis superimposed in the post-buckling regime.

4. Results and Analysis

4.1 Analysis of post-buckling results

In this section, we present the results of an example case of the post-buckling analysis. We illustrate the result with an example of the particulate composite with the spacing ratio $\xi = 0.45$ and periodicity aspect ratio $\eta = 6$. The corresponding initial RVE at $\varepsilon = 0$ is shown in Fig. 4. Note that, only 80 unit cells of the RVE are displayed for a more compact illustration here and thereafter. We observe that the composite maintains a straight column of inclusions until it reaches the onset of the first stage buckling at the corresponding critical strain level of $\varepsilon_I^{cr} = 0.233$. At this point, the inclusion column experiences a sudden local collapse, with adjacent inclusions moving to the opposite side of each other. For example, as shown in Fig. 4, corresponding to $\varepsilon = 0.368$, the odd-numbered inclusions from the bottom move horizontally to the right side, while the even-numbered inclusions move to the left. As the compression continues to increase despite the buckling already being triggered, the composite structure quickly forms a seemingly "two straight columns of inclusions" near the middle line of the RVE (see, for example, in Fig. 4, corresponding to $\varepsilon = 0.555$). This post-buckling pattern, however, provides a highly ordered and compact arrangement of inclusions. Note that this composite,

after the buckling-induced particle rearrangements, becomes stable again. The newly formed configuration contains an effective particle-reinforced composite layer, now including the two columns of inclusions surrounded by the soft matrix (see, for example, the composite structure corresponding to $\varepsilon_{II}^{cr} = 0.555$ in Fig. 4). Interestingly, with further deformation, this reinforced layer experiences a wrinkling-like instability after the new (second) critical strain level of $\varepsilon_{II}^{cr} = 0.555$ is reached. At this point, the two "straight columns" of inclusions transform into a complex "chain" of inclusions. This pattern transformation can be observed in the deformed RVE shown in Fig. 4, corresponding to $\varepsilon = 0.565$. We refer to such loss of stability in the post-buckling regime (after the first or initial buckling) as the secondary buckling.

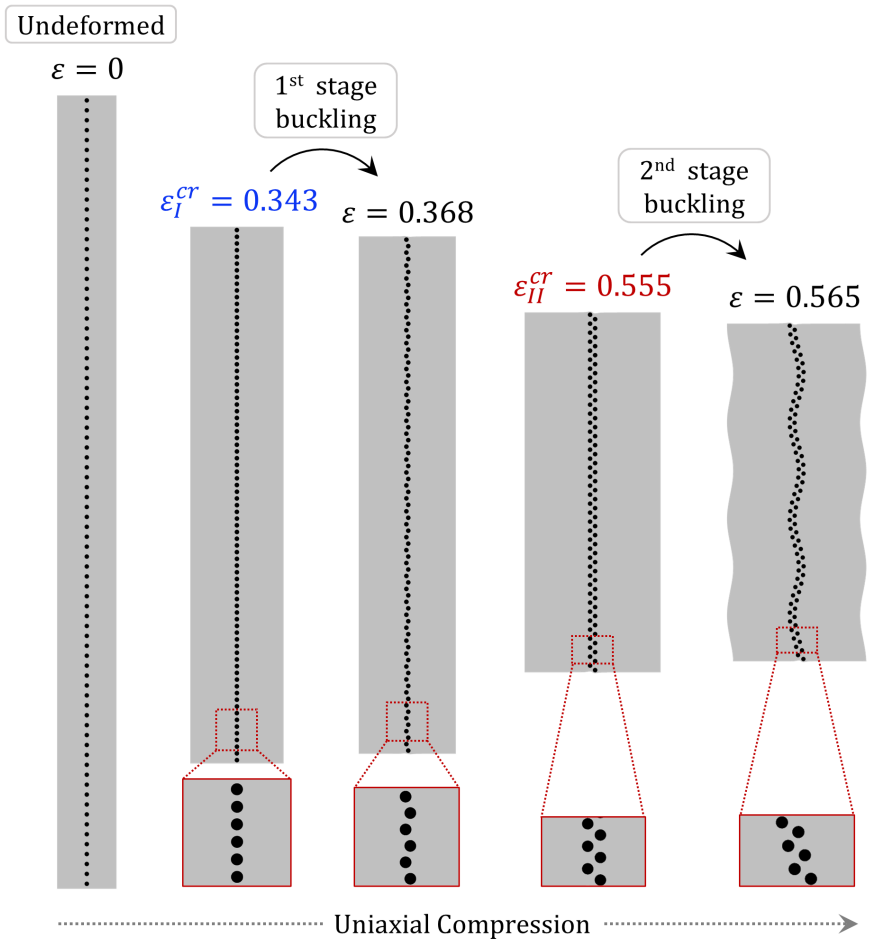

Fig. 4 The deformation sequence under the compressive strain level $\varepsilon = 0$, $\varepsilon = 0.343$, $\varepsilon = 0.368$, $\varepsilon = 0.555$, and $\varepsilon = 0.565$; initial geometric parameters are $\xi = 0.45$ and $\eta = 6$. Only 80 unit cells of the RVE are displayed for a more compact illustration.

Next, in Fig. 5, we illustrate the results of the DFT analysis for the composite with $\xi =$

0.45 and $\eta = 6$, showing the dependence of the Fourier coefficient f on component wavenumbers, for fixed compressive strain levels from 0 to 0.557. Until the critical strain level $\varepsilon^{cr} = 0.343$, the composite maintains a straight column of inclusions, and correspondingly, all component wavenumbers are characterized by nearly zero Fourier coefficients. However, after reaching the first critical strain level ($\varepsilon_I^{cr} = 0.343$), the inclusion column suddenly collapses and transforms into a periodicity-doubling pattern. Correspondingly, a peak Fourier coefficient emerges at $k = 0.5$, representing the doubled periodicity and the critical wavenumber of the first buckling $k_I^{cr} = 0.5$. This is illustrated by the green curve with triangular markers shown in Fig. 5 corresponding to $\varepsilon = 0.368$.

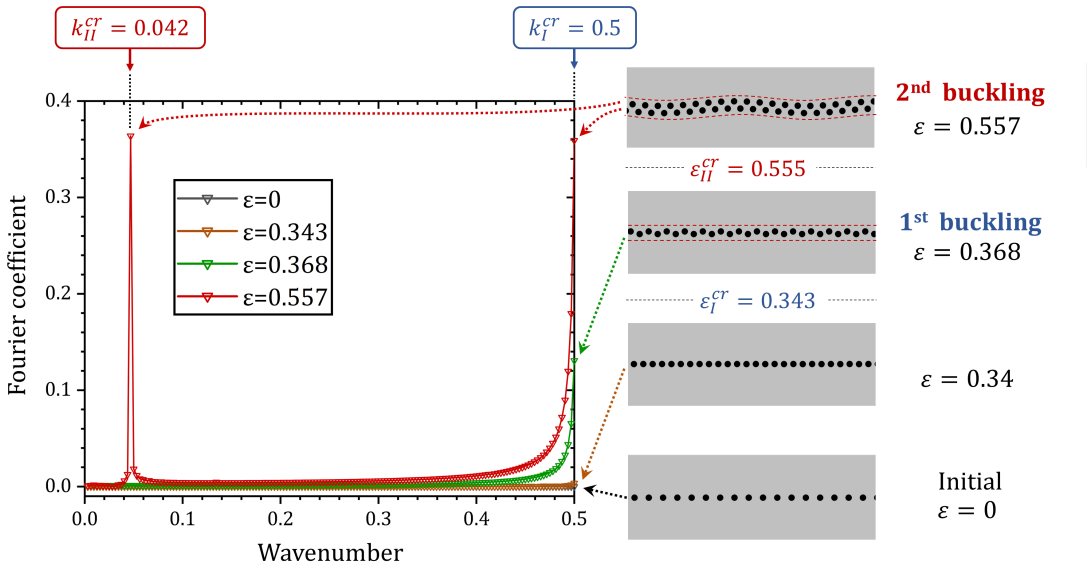

Fig. 5 The DFT analysis results of the post-buckling development for the composite with a spacing ratio $\xi = 0.45$ and periodicity aspect ratio $\eta = 6$ at compressive strain $\varepsilon = 0$, $\varepsilon = 0.34$, $\varepsilon = 0.368$, and $\varepsilon = 0.557$ with $N = 320$ number of unit cells built in the RVE (the RVE view is zoomed so not all inclusions are displayed).

Next, with an increase in the compressive strain level, the post-buckling pattern evolves, and the thickness of the "particle-reinforced layer" increases. After the critical strain of the secondary buckling $\varepsilon_{II}^{cr} = 0.55$, we observe a second peak emerging in the Fourier spectrum at $k_{II}^{cr} = 0.042$, representing a wavy buckling mode of the "reinforced layer." Therefore, $k_{II}^{cr} = 0.042$ is identified as the critical wavenumber of the secondary buckling. Correspondingly, the critical strain of the secondary buckling ε_{II}^{cr} is identified at the lowest strain level, where a peak in the Fourier spectrum is detected to exceed the threshold coefficient

10^{-2} at a wavenumber other than $k_I^{cr} = 0.5$.

4.2 Dependence of critical strains on geometric parameters

We start by examining the *secondary* buckling development via the dependence of critical strains on the composite's initial geometrical parameters. Fig. 6 shows the dependence of the critical strain on the periodicity aspect ratio η for various fixed values of the inclusion spacing ratios $\xi = 0.3, 0.35, 0.4$ and 0.45, where the dotted and continuous curves correspond to longwave ($k_{II}^{cr} \to 0$) and microscopic ($k_{II}^{cr} > 0$) buckling derived from the Bloch Floquet analysis, respectively; the triangular markers correspond to the results from the post-buckling analysis. It should be emphasized that *secondary* buckling has only been found in composites with "periodicity-doubling" buckling mode in their *first* buckling stage. It has been shown in recent research (Chen et al., 2022, 2023) that those "periodicity-doubling" patterns form in composites with small enough spacing ratios ($\xi \lesssim 0.45$) and large enough periodicity aspect ratios (for composites with $\xi = 0.45$, the "periodicity-doubling" pattern is found when $\eta \gtrsim 2$). Moreover, the admissible geometries are restricted by $d < b$ and $d < a$, thus, limiting the parameter space as $\eta > \xi$.

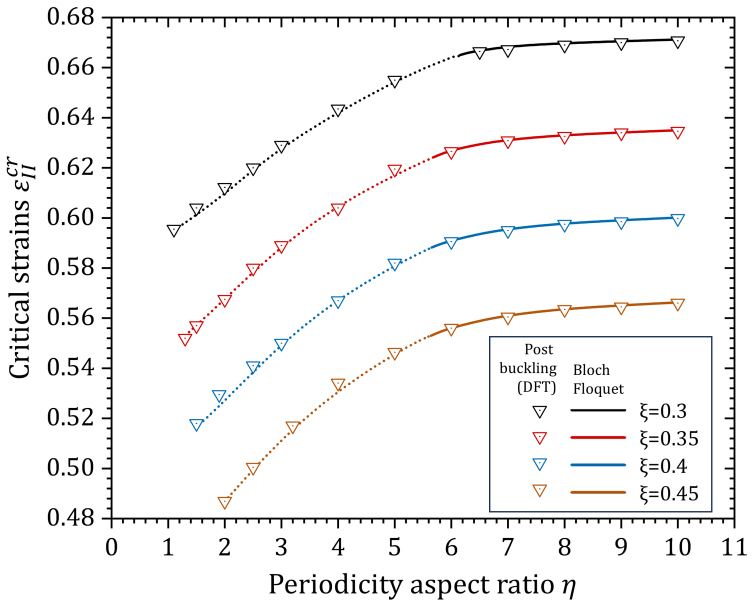

Fig. 6 The dependence of *secondary* buckling critical strain on periodicity aspect ratio with various spacing ratios. The dotted and continuous curves correspond to longwave and microscopic buckling results from the Bloch-Floquet analysis, respectively; the triangular markers correspond to results from the post-buckling DFT analysis.

We observe that the secondary buckling critical strain derived from post-buckling analysis agrees well with the predictions of the Bloch-Floquet analysis. The composites with higher spacing ratios experience secondary buckling at lower compressive strains. For example, as shown in Fig. 6, in the composites with the same periodicity aspect ratio $\eta = 7$, with an increase in the spacing ratio from $\xi = 0.3$ to $\xi = 0.45$, the onset of *secondary* buckling shifts from $\varepsilon_{II}^{cr} = 0.669$ to 0.561. This stems from the fact that the large-sized inclusions (that are large in the composites with larger spacing ratios) provide a high volume fraction of the stiff inclusions in the effective particle-reinforced layer, thus increasing the effective stiffness contrast between the soft matrix and the particle-reinforced layer, eventually leading to an earlier onset of the secondary buckling. We also observed that the critical strain ε_{II}^{cr} increases monotonically with an increase in η for all considered spacing ratios. Moreover, we observe that the secondary buckling develops in the longwave modes ($k_{II}^{cr} \to 0$) in the composites with small enough periodicity aspect ratios. However, the buckling mode switches from longwave to microscopic ones in composites with a periodicity aspect ratio large than a threshold value η^{th}, dictated by the initial spacing ratio value ξ (specifically, larger spacing ratios lead to an earlier transition from micro- to longwave secondary buckling). For example, for the composite with $\xi = 0.35$ (the red curve in Fig. 6), the buckling develops in a longwave mode with small enough periodicity aspect ratios, such as $\eta = 3$. With an increase in η, the critical strain increases monotonically. After the threshold value $\eta^{th} \approx 5.68$ is reached, a switch from the longwave to microscopic buckling mode occurs, followed by the continuous increase of the critical strain with an increase in the periodicity aspect ratio.

4.3 Dependence of secondary buckling critical wavenumbers on geometric parameters

Let us examine the dependence of the secondary buckling critical wavenumber on the periodicity aspect ratio η. In Fig. 7, we plot the prediction of k_{II}^{cr} from Bloch-Floquet analysis (red dotted and continuous curves, corresponding to longwave and microscopic buckling, respectively) and the post-buckling results (triangular markers). We observe that the Bloch-Floquet and the post-buckling predictions agree well. Specifically, for microscopic instabilities, they predict critical wavenumbers at a finite value $k_{II}^{cr} > 0$; for longwave instabilities, they predict critical wavenumbers corresponding to their longwave limit $k_{II}^{cr} \to 0$ and $k_{II}^{cr} =$

$1/320$, respectively.

The good agreement between the Bloch–Floquet analysis and the post-buckling analysis, despite the incommensurate buckling mode where k_{II}^{cr} does not correspond to an integer multiple of the initial primitive cells, indicates that the initial buckling mode predicted by the Bloch–Floquet analysis is sufficiently stable and does not evolve divergently during the post-buckling process. This stability can be attributed to two factors: 1) the large wavelength of the secondary buckling mode (in most cases $k_{II}^{cr} < 1/12$), and 2) the transformation of the reinforced region into two interlaced columns of inclusions, making the stiffness distribution more uniform along the loading direction, causing the structure to behave more like a layered composite.

Next, when the periodicity aspect ratio increases beyond a threshold value η^{th} (corresponding to the initial inclusion columns placed farther away enough from each other), we find a transition from longwave instability to microscopic instability (corresponding to $k_{II}^{cr} > 0$ in Bloch-Floquet analysis and $k_{II}^{cr} > 1/320$ in post-buckling analysis). We also observe that the composites with larger spacing ratios experience an earlier transition from longwave to microscopic instabilities, but the corresponding critical wavenumber increases at a relatively lower rate. For example, in composites with $\xi = 0.3$ and $\xi = 0.4$, the switch from longwave to microscopic mode occurs at $\eta^{th} \approx 6.18$ and $\eta^{th} \approx 5.65$, respectively. After those switches, the wavenumber starts to increase. However, at a higher critical wavenumber, such as $\eta = 10$, the composite with $\xi = 0.3$ reaches a lower critical wavenumber $k_{II}^{cr} = 0.074$ while the composite with $\xi = 0.4$ reaches a higher critical wavenumber $k_{II}^{cr} = 0.069$. However, for composites with a larger spacing ratio, such as $\xi = 0.45$, the corresponding threshold value shifts down to $\eta^{th} \approx 5.65$; the critical wavenumber reduces to $k_{II}^{cr} = 0.137$ at $\eta = 10$.

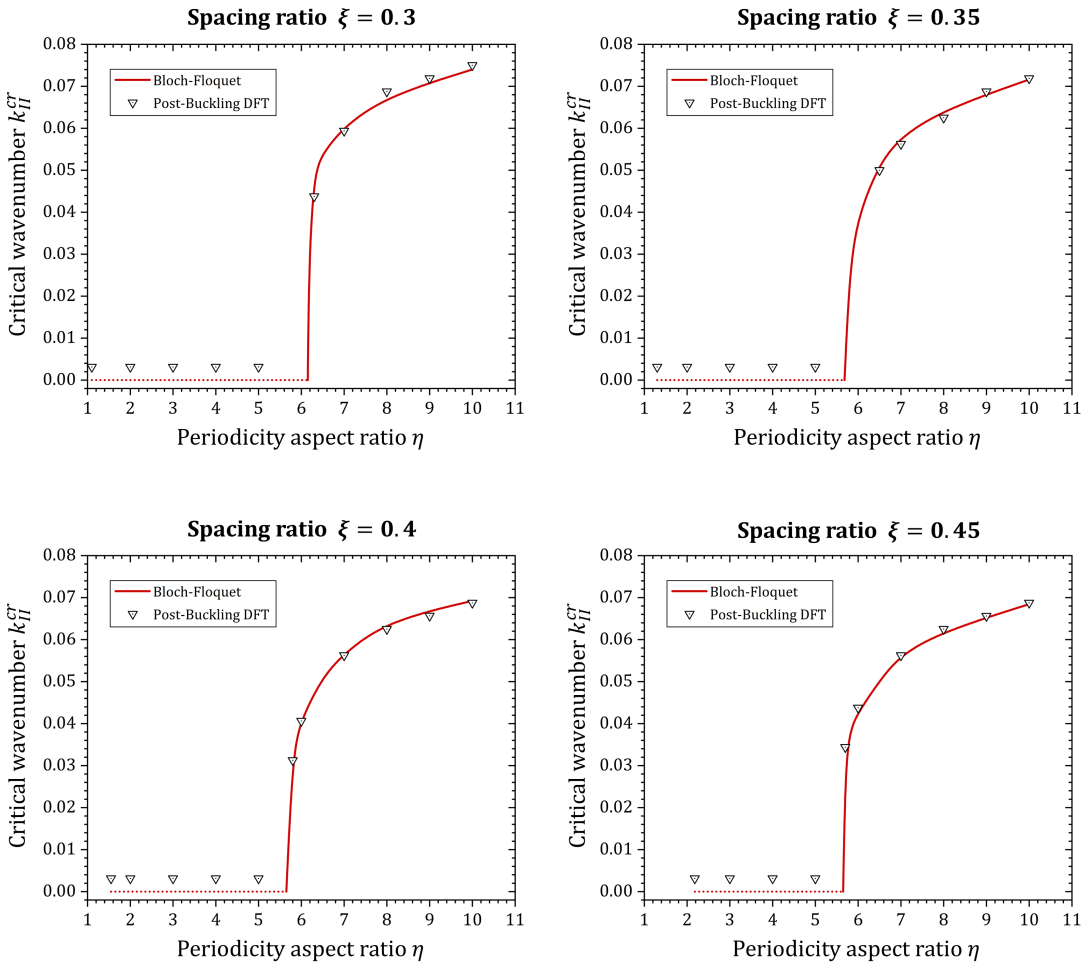

Fig. 7 The dependence of the critical wavenumber on the periodicity aspect ratio with various spacing ratios. Triangular markers and continuous curves correspond to results from post-buckling DFT analysis and Bloch Floquet analysis, respectively.

Finally, we summarize the results of the first and secondary buckling patterns as a map in the geometrical parameter space of the periodicity aspect ratio η and the spacing ratio ξ, as shown in Fig. 8. In the map, the *first stage* buckling patterns are divided into *six* sub-domains. Among them, four grey sub-domains represent composite geometries that will only develop the first stage buckling (Chen et al., 2023): (i) the domain labeled as the "zigzag chain" corresponds to the critical wavenumber of the first stage buckling $k_I^{cr} \to 0$, where buckling pattern is a single zigzag chain of inclusions; (ii) the domain labeled with "Wavy chain" corresponds to relatively low k_I^{cr} from 0 to the vicinity of 0.25, where the buckling pattern is a "wave-like chain" of inclusions; (iv) the domain labeled with "Superimposed" corresponds to a relatively high k_I^{cr} from approximately 0.25 to 0.4, where the buckling pattern exhibits a superposition of wavelets (in small length scales) in between envelopes in large length scales. The highlighted

two sub-domains represent composite geometries that can develop the *secondary* buckling, based on their formation of a "periodicity-doubling" or "adapted periodicity-doubling" pattern in the first-stage buckling. In particular, the "adapted periodicity-doubling" sub-domain includes special cases that cannot be predicted by Bloch–Floquet analysis, as the post-buckling pattern diverges from the linearized BF prediction. However, these cases can be captured by DFT analysis, corresponding to the first-stage buckling modes characterized by a single dominant peak at wavenumber 0.5.

The bright blue domain – labeled with "longwave" – represents the geometries that will develop longwave secondary buckling, corresponding to $k_{II}^{cr} \to 0$; the dark blue domain – labeled as "microscopic," represents the composite geometries that will develop secondary buckling in the microscopic modes, corresponding to $k_{II}^{cr} > 0$. Our results have shown that *secondary* buckling occurs in composites with small aspect ratios and large periodicity aspect ratios, in which longwave secondary buckling occurs with relatively small periodicity aspect ratios, and microscopic secondary buckling occurs with relatively large spacing ratios.

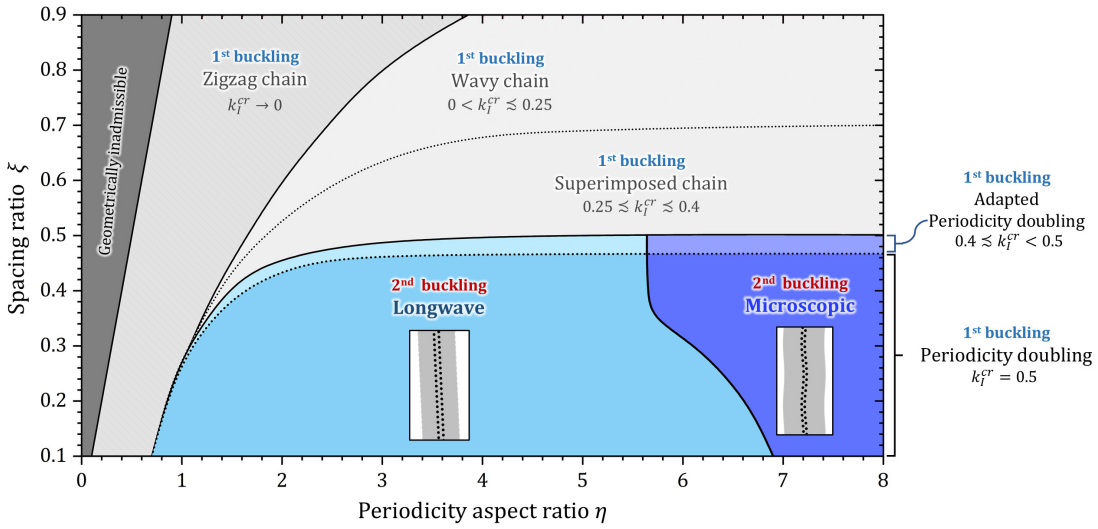

Fig. 8 The first and secondary buckling pattern mapping in the geometrical parameter space. The highlighted areas (bright and dark blue) represent the secondary buckling.

Conclusion

We reported the numerical observations of a distinctive phenomenon – the development of *secondary* buckling in soft particulate composites. Our findings demonstrate that the further evolution of deformation in the post-buckling regime can lead to a secondary buckling, but this

occurs only when the first-stage buckling exhibits a “periodicity-doubling” or “adapted periodicity-doubling” pattern, which corresponds to the DFT analysis of the first-stage buckling showing a single dominant peak at wavenumber 0.5.

This secondary buckling gives rise to a new array of instability patterns. Specifically, in some particulate composites, we have observed the formation of the effective particle-reinforced layer in their post-buckling regime, followed by wrinkling of this reinforced layer after the secondary critical strain is reached.

The secondary buckling gives rise to the development of two types of patterns: the longwave (or macroscopic) and the microscopic buckling, determined by the initial composite geometry. To characterize the secondary buckling development, we performed the finite-amplitude post-buckling and Bloch Floquet analyses in the post-buckling regime of the soft composites. The dependencies of critical instability characteristics on geometrical parameters derived from the two independent analyses are in good agreement. Finally, we have investigated the transition of secondary buckling patterns from a longwave pattern to a microscopic pattern characterized by its critical wavenumber with a variation in the geometrical parameters.

The complex post-buckling behavior can be further enriched through external stimuli, such as, for example, electric (Liu et al., 2021; Goshkoderia et al., 2020; Xia et al., 2019) or magnetic fields (Saxena et al., 2013, 2014; Garcia-Gonzalez et al., 2023; Lucarini et al., 2022; Moreno-Mateos et al., 2022; Psarra et al., 2017; Mukherjee et al., 2021; Danas, et al., 2012) in active materials. Furthermore, the secondary buckling phenomenon may also result in complex unloading behavior in soft composites, thus potentially enriching the resilience and energy dissipation capabilities in soft heterogeneous materials (Lee et al., 2023; Shan et al., 2015).

We note that soft composites (especially, natural composites) may possess geometrical (Chen et al., 2019; Ding et al., 2019; Yu et al., 2022) or material (Hauseux et al., 2017, 2018; Rappel et al., 2019) imperfections and uncertainties. Such uncertainties may influence the prediction of the composites buckling behavior. To thoroughly understand and quantify the impact of these uncertainties on the composites behavior, multi-field coupled stochastic analyses can be employed (Elouneg et al., 2021; Mazier et al., 2022).

To summarize, as the field has predominantly concentrated on the first buckling stage of particulate composites, this study, as the first report, numerically revealed the distinctive

secondary buckling phenomenon in soft particulate composites. Our finding of secondary buckling in soft particulate composites shows that the system can switch among three functional configurations instead of two, thereby broadening the switchable design space of soft composite materials. This phenomenon also broadens the set of new patterns and associated behaviors and potentially expands the design space for other tunable and switchable materials.

Acknowledgments

Data Availability: The data required to reproduce these findings cannot be shared at this time due to technical or time limitations.

References

[1] Aboudi, J., & Gilat, R. (2023). Bifurcation buckling and the effect of imperfections on the microbuckling of soft materials with periodic microstructure by the finite strain HFGMC micromechanics. International Journal of Solids and Structures, 270, 112227.

[2] Aboudi, J., & Volokh, K. Y. (2020). Modeling deformation and failure of viscoelastic composites at finite strains. Mechanics of Soft Materials, 2, 1-19.

[3] Arora, N., Yao, Q., & Rudykh, S. (2022a). Deformation activated negative group velocity state in soft laminates. Extreme Mechanics Letters, 51, 101592.

[4] Arora, N., Li, J., & Rudykh, S. (2022b). Tunable buckling configurations via in-plane periodicity in soft 3D-fiber composites: Simulations and experiments. International Journal of Solids and Structures, 250.

[5] Bertoldi, K., Boyce, M. C., Deschanel, S., Prange, S. M., & Mullin, T. (2008). Mechanics of deformation-triggered pattern transformations and superelastic behavior in periodic elastomeric structures. Journal of the Mechanics and Physics of Solids, 56(8), 2642–2668.

[6] Bertoldi, K., Reis, P. M., Willshaw, S., & Mullin, T. (2010). Negative Poissons ratio behavior induced by an elastic instability. Advanced materials, 22(3), 361-366.

[7] Bruno, D., Greco, F., Lonetti, P., Blasi, P. N., & Sgambitterra, G. (2010). An investigation on microscopic and macroscopic stability phenomena of composite solids with periodic microstructure. International Journal of Solids and Structures, 47(20), 2806–2824.

[8] Chen, D., Arora, N., Xiang, Y., Li, J., Slesarenko, V., & Rudykh, S. (2022). Instability-

induced patterns and their post-buckling development in soft particulate composites. Mechanics of Materials, 175, 104482.

[9] Chen, D., Xiang, Y., Arora, N., Yao, Q., Li, J., & Rudykh, S. (2023). Post-buckling development in soft particulate composites. Composite Structures, 117337.

[10] Chen, L. L., Lian, H., Liu, Z., Chen, H. B., Atroshchenko, E., & Bordas, S. P. A. (2019). Structural shape optimization of three dimensional acoustic problems with isogeometric boundary element methods. Computer Methods in Applied Mechanics and Engineering, 355, 926–951.

[11] Combescure, C., Henry, P., & Elliott, R. S. (2016). Post-bifurcation and stability of a finitely strained hexagonal honeycomb subjected to equi-biaxial in-plane loading. International Journal of Solids and Structures, 88, 296-318.

[12] Danas, K., Kankanala, S. V., & Triantafyllidis, N. (2012). Experiments and modeling of iron-particle-filled magnetorheological elastomers. Journal of the Mechanics and Physics of Solids, 60(1), 120-138.

[13] De Maio, U., Greco, F., Luciano, R., Sgambitterra, G., & Pranno, A. (2023). Microstructural design for elastic wave attenuation in 3D printed nacre-like bioinspired metamaterials lightened with hollow platelets. Mechanics Research Communications, 104045.

[14] Ding, C., Deokar, R. R., Ding, Y., Li, G., Cui, X., Tamma, K. K., & Bordas, S. P. A. (2019). Model order reduction accelerated Monte Carlo stochastic isogeometric method for the analysis of structures with high-dimensional and independent material uncertainties. Computer Methods in Applied Mechanics and Engineering, 349, 266–284.

[15] Ehret, A. E., & Itskov, M. (2007). A polyconvex hyperelastic model for fiber-reinforced materials in application to soft tissues. Journal of Materials Science, 42, 8853-8863.

[16] Elouneg, A., Sutula, D., Chambert, J., Lejeune, A., Bordas, S. P. A., & Jacquet, E. (2021). An open-source FEniCS-based framework for hyperelastic parameter estimation from noisy full-field data: Application to heterogeneous soft tissues. Computers and Structures, 255.

[17] Galich, P. I., Slesarenko, V., Li, J., & Rudykh, S. (2018). Elastic instabilities and shear waves in hyperelastic composites with various periodic fiber arrangements. International

570 Journal of Engineering Science, 130, 51–61.
571 [18] Gao, N., Li, J., Bao, R. H., & Chen, W. Q. (2019). Harnessing uniaxial tension to tune
572 Poisson's ratio and wave propagation in soft porous phononic crystals: an experimental
573 study. Soft Matter, 15(14), 2921–2927.
574 [19] Geymonat, G., Müller, S., & Triantafyllidis, N. (1993). Homogenization of nonlinearly
575 elastic materials, microscopic bifurcation and macroscopic loss of rank-one convexity.
576 Archive for Rational Mechanics and Analysis, 122(3), 231–290.
577 [20] Goshkoderia, A., Chen, V., Li, J., Juhl, A., Buskohl, P., & Rudykh, S. (2020). Instability-
578 Induced Pattern Formations in Soft Magnetoactive Composites. Physical Review Letters,
579 124(15), 1–7.
580 [21] Greco, F., & Luciano, R. (2011). A theoretical and numerical stability analysis for
581 composite micro-structures by using homogenization theory. Composites Part B:
582 Engineering, 42(3), 382-401.
583 [22] Greco, F., Leonetti, L., De Maio, U., Rudykh, S., & Pranno, A. (2021). Macro- and
584 micro-instabilities in incompressible bioinspired composite materials with nacre-like
585 microstructure. Composite Structures, 269.
586 [23] Greco, F., Lonetti, P., Luciano, R., Blasi, P. N., & Pranno, A. (2018). Nonlinear effects in
587 fracture induced failure of compressively loaded fiber reinforced composites. Composite
588 Structures, 189, 688-699.
589 [24] Garcia-Gonzalez, D., Ter-Yesayants, T., Moreno-Mateos, M. A., & Lopez-Donaire, M. L.
590 (2023). Hard-magnetic phenomena enable autonomous self-healing elastomers.
591 Composites Part B: Engineering, 248, 110357.
592 [25] Hauseux, P., Hale, J. S., & Bordas, S. P. A. (2017). Accelerating Monte Carlo estimation
593 with derivatives of high-level finite element models. Computer Methods in Applied
594 Mechanics and Engineering, 318, 917–936.
595 [26] Hauseux, P., Hale, J. S., Cotin, S., & Bordas, S. P. A. (2018). Quantifying the uncertainty
596 in a hyperelastic soft tissue model with stochastic parameters. Applied Mathematical
597 Modelling, 62, 86–102.
598 [27] Li, J., & Rudykh, S. (2019b). Tunable microstructure transformations and auxetic
599 behavior in 3D-printed multiphase composites: The role of inclusion distribution.

600 Composites Part B: Engineering, 172, 352–362.
601 [28] Li, J., Arora, N., & Rudykh, S. (2021). Elastic instabilities, microstructure
602 transformations, and pattern formations in soft materials. Current Opinion in Solid State
603 and Materials Science, 25(2), 100898.
604 [29] Li, J., Pallicity, T. D., Slesarenko, V., Goshkoderia, A., & Rudykh, S. (2019a). Domain
605 formations and pattern transitions via instabilities in soft heterogeneous materials.
606 Advanced Materials, 31(14), 1807309.
607 [30] Li, J., Slesarenko, V., & Rudykh, S. (2018b). Auxetic multiphase soft composite material
608 design through instabilities with application for acoustic metamaterials. Soft Matter,
609 14(30), 6171–6180.
610 [31] Li, J., Slesarenko, V., & Rudykh, S. (2019d). Microscopic instabilities and elastic wave
611 propagation in finitely deformed laminates with compressible hyperelastic phases.
612 European Journal of Mechanics, A/Solids, 73, 126–136.
613 [32] Li, J., Slesarenko, V., & Rudykh, S. (2022). Emergence of instability-driven domains in
614 soft stratified materials. npj Computational Materials, 8(1), 100.
615 [33] Li, J., Slesarenko, V., Galich, P. I., & Rudykh, S. (2018a). Instabilities and pattern
616 formations in 3D-printed deformable fiber composites. Composites Part B: Engineering,
617 148, 114–122.
618 [34] Li, J., Wang, Y., Chen, W., Wang, Y. S., & Bao, R. (2019c). Harnessing inclusions to tune
619 post-buckling deformation and bandgaps of soft porous periodic structures. Journal of
620 Sound and Vibration, 459, 114848.
621 [35] Li, Y., Kaynia, N., Rudykh, S., & Boyce, M. C. (2013). Wrinkling of interfacial layers in
622 stratified composites. Advanced Engineering Materials, 15(10), 921–926.
623 [36] Lee, G., Lee, J., Lee, S., Rudykh, S., & Cho, H. (2023). Extreme resilience and
624 dissipation in heterogeneous elasto-plastomeric crystals. Soft Matter.
625 [37] Lucarini, S., Hossain, M., & Garcia-Gonzalez, D. (2022). Recent advances in hard-
626 magnetic soft composites: Synthesis, characterisation, computational modelling, and
627 applications. Composite Structures, 279, 114800.
628 [38] Liu, Z., McBride, A., Sharma, B. L., Steinmann, P., & Saxena, P. (2021). Coupled
629 electro-elastic deformation and instabilities of a toroidal membrane. Journal of the

630 Mechanics and Physics of Solids, 151, 104221.
631 [39] Moreno-Mateos, M. A., Hossain, M., Steinmann, P., & Garcia-Gonzalez, D. (2022).
632 Hybrid magnetorheological elastomers enable versatile soft actuators. npj Computational
633 Materials, 8(1), 162.
634 [40] Melnikov, A., Ogden, R. W., Dorfmann, L., & Merodio, J. (2021). Bifurcation analysis of
635 elastic residually-stressed circular cylindrical tubes. International Journal of Solids and
636 Structures, 226–227, 111062.
637 [41] Merodio, J., & Ogden, R. W. (2002). Material instabilities in fiber-reinforced nonlinearly
638 elastic solids under plane deformation. Archives of Mechanics, 54(5–6), 525–552.
639 [42] Merodio, J., & Ogden, R. W. (2003). Instabilities and loss of ellipticity in fiber-
640 reinforced compressible non-linearly elastic solids under plane deformation. International
641 Journal of Solids and Structures, 40(18), 4707–4727.
642 [43] Merodio, J., & Ogden, R. W. (2005a). Remarks on instabilities and ellipticity for a fiber-
643 reinforced compressible nonlinearly elastic solid under plane deformation. Quarterly of
644 applied mathematics, 63(2), 325-333.
645 [44] Merodio, J., & Ogden, R. W. (2005b). Tensile instabilities and ellipticity in fiber-
646 reinforced compressible non-linearly elastic solids. International Journal of Engineering
647 Science, 43(8-9), 697-706.
648 [45] Merodio, J., & Pence, T. J. (2001a). Kink surfaces in a directionally reinforced neo-
649 Hookean material under plane deformation: I. Mechanical equilibrium. Journal of
650 Elasticity, 62, 119-144.
651 [46] Merodio, J., & Pence, T. J. (2001b). Kink surfaces in a directionally reinforced neo-
652 Hookean material under plane deformation: II. Kink band stability and maximally
653 dissipative band broadening. Journal of Elasticity, 62, 145-170.
654 [47] Mullin, T., Deschanel, S., Bertoldi, K., & Boyce, M. C. (2007). Pattern transformation
655 triggered by deformation. Physical Review Letters, 99(8).
656 [48] Mukherjee, D., Rambausek, M., & Danas, K. (2021). An explicit dissipative model for
657 isotropic hard magnetorheological elastomers. Journal of the Mechanics and Physics of
658 Solids, 151, 104361.
659 [49] Mazier, A., Bilger, A., Forte, A. E., Peterlik, I., Hale, J. S., & Bordas, S. P. A. (2022).

660 Inverse deformation analysis: an experimental and numerical assessment using the
661 FEniCS Project. Engineering with Computers.
662 [50] Ogden, R. W. (1997). Non-linear elastic deformations, Dover Publication, Mineola, New
663 York.
664 [51] Okumura, D., Ohno, N., & Noguchi, H. (2002). Post-buckling analysis of elastic
665 honeycombs subject to in-plane biaxial compression. International journal of solids and
666 structures, 39(13-14), 3487-3503.
667 [52] Papka, S. D., & Kyriakides, S. (1999a). Biaxial crushing of honeycombs:—Part 1:
668 Experiments. International Journal of Solids and Structures, 36(29), 4367-4396.
669 [53] Papka, S. D., & Kyriakides, S. (1999b). In-plane biaxial crushing of honeycombs—: Part
670 II: Analysis. International Journal of Solids and Structures, 36(29), 4397-4423.
671 [54] Psarra, E., Bodelot, L., & Danas, K. (2017). Two-field surface pattern control via
672 marginally stable magnetorheological elastomers. Soft Matter, 13(37), 6576-6584.
673 [55] Pranno, A., Greco, F., Leonetti, L., Lonetti, P., Luciano, R., & De Maio, U. (2022). Band
674 gap tuning through microscopic instabilities of compressively loaded lightened nacre-like
675 composite metamaterials. Composite Structures, 282, 115032.
676 [56] Qiu, G. Y., & Pence, T. J. (1997). Loss of ellipticity in plane deformation of a simple
677 directionally reinforced incompressible nonlinearly elastic solid. Journal of Elasticity, 49,
678 31-63.
679 [57] Rafsanjani, A., Bertoldi, K., & Studart, A. R. (2019). Programming soft robots with
680 flexible mechanical metamaterials. Science Robotics, 4(29), eaav7874.
681 [58] Rudykh, S., & Boyce, M. C. (2014). Transforming wave propagation in layered media
682 via instability-induced interfacial wrinkling. Physical Review Letters, 112(3).
683 [59] Rudykh, S., & Debotton, G. (2012). Instabilities of hyperelastic fiber composites:
684 Micromechanical versus numerical analyses. Journal of Elasticity, 106(2), 123–147.
685 [60] Rappel, H., Beex, L. A., Noels, L., & Bordas, S. P. A. (2019). Identifying elastoplastic
686 parameters with Bayes' theorem considering output error, input error and model
687 uncertainty. Probabilistic Engineering Mechanics, 55, 28-41.
688 [61] Saxena, P., Hossain, M., & Steinmann, P. (2013). Mathematical modelling of finite strain
689 magneto-viscoelastic deformations. PAMM, 13(1), 163-164.

690 [62] Saxena, P., Hossain, M., & Steinmann, P. (2014). Nonlinear magneto-viscoelasticity of
691 transversally isotropic magneto-active polymers. Proceedings of the Royal Society A:
692 Mathematical, Physical and Engineering Sciences, 470(2166), 20140082.
693 [63] Shan, S., Kang, S. H., Wang, P., Qu, C., Shian, S., Chen, E. R., & Bertoldi, K. (2014).
694 Harnessing Multiple Folding Mechanisms in Soft Periodic Structures for Tunable Control
695 of Elastic Waves. Advanced Functional Materials, 24(31), 4935–4942.
696 [64] Shan, S., Kang, S. H., Raney, J. R., Wang, P., Fang, L., Candido, F., ... & Bertoldi, K.
697 (2015). Multistable architected materials for trapping elastic strain energy. *Adv.*
698 *Mater*, *27*(29), 4296-4301.
699 [65] Slesarenko, V., & Rudykh, S. (2016). Harnessing viscoelasticity and instabilities for
700 tuning wavy patterns in soft layered composites. Soft Matter, 12(16), 3677–3682.
701 [66] Slesarenko, V., Galich, P. I., Li, J., Fang, N. X., & Rudykh, S. (2018). Foreshadowing
702 elastic instabilities by negative group velocity in soft composites. Applied Physics
703 Letters, 113(3).
704 [67] Triantafyllidis, N., Nestorović, M. D., & Schraad, M. W. (2006). Failure Surfaces for
705 Finitely Strained Two-Phase Periodic Solids Under General In-Plane Loading. Journal of
706 Applied Mechanics, 73(3), 505–515.
707 [68] Volokh, K. Y. (2017). Loss of ellipticity in elasticity with energy limiters. European
708 Journal of Mechanics-A/Solids, 63, 36-42.
709 [69] Wang, P., Casadei, F., Shan, S., Weaver, J. C., & Bertoldi, K. (2014). Harnessing
710 Buckling to Design Tunable Locally Resonant Acoustic Metamaterials. Physical Review
711 Letters, 113(1), 014301.
712 [70] Xiang, Y., Schilling, C., Arora, N., Boydston, A. J., & Rudykh, S. (2020a). Mechanical
713 characterization and constitutive modeling of visco-hyperelasticity of photocured
714 polymers. Additive Manufacturing, 36, 101511.
715 [71] Xiang, Y., Zhong, D., Rudykh, S., Zhou, H., Qu, S., & Yang, W. (2020b). A Review of
716 Physically Based and Thermodynamically Based Constitutive Models for Soft Materials.
717 Journal of Applied Mechanics, Transactions ASME, 87(11), 110801.
718 [72] Xiang, Y., Chen, D., Arora, N., Yao, Q., & Rudykh, S. (2023). Towards understanding the
719 role of viscoelasticity in microstructural buckling in soft particulate composites.

720 Composites Part B: Engineering, 110850.
721 [73] Xia, X., Afshar, A., Yang, H., Portela, C. M., Kochmann, D. M., Di Leo, C. V., & Greer,
722 J. R. (2019). Electrochemically reconfigurable architected materials. Nature, 573(7773),
723 205-213.
724 [74] Yu, P., Bordas, S. P. A., & Kerfriden, P. (2022). Adaptive Isogeometric analysis for
725 transient dynamics: Space–time refinement based on hierarchical a-posteriori error
726 estimations. Computer Methods in Applied Mechanics and Engineering, 394, 114774.